Modulating Meltpool Dynamics and Microstructure using Thermoelectric Magnetohydrodynamics in Additive Manufacturing

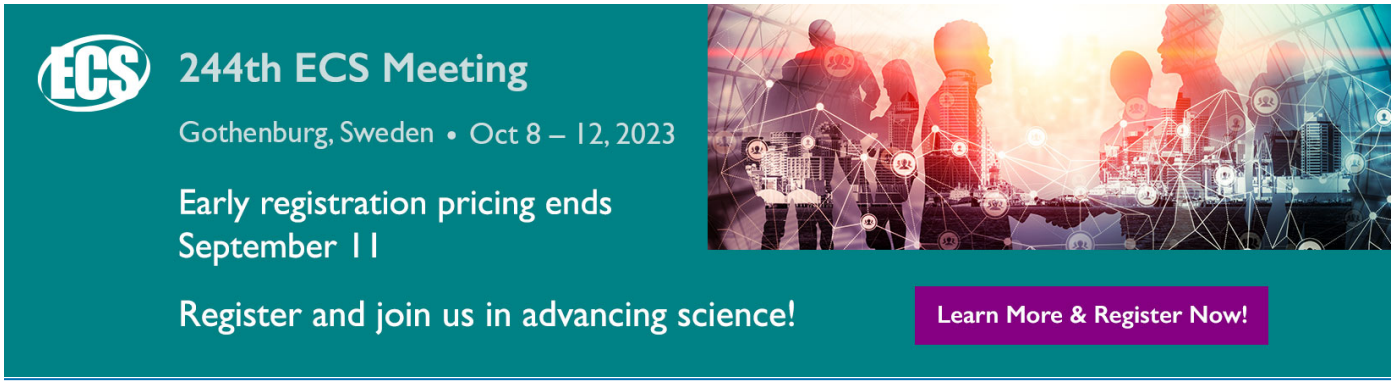

Modulating Meltpool Dynamics and Microstructure using Thermoelectric Magnetohydrodynamics in Additive Manufacturing

A Kao[1], C Tonry[1], P Soar[1], I Krastins[1,2], X Fan[3], PD Lee[3] and K Pericleous[1]

[1]Computational Science and Engineering Group, University of Greenwich, UK
[2]Institute of Physics, University of Latvia, Jelgavas iela 3, Riga, LV-1004, Latvia
[3]Department of Mechanical Engineering, UCL, UK

Email: a.kao@gre.ac.uk

Abstract. Meltpool modulation in Selective Laser Remelting Additive Manufacturing via an oscillating magnetic field generates Thermoelectric Magnetohydrodynamics (TEMHD) flow. Numerical predictions show that the resulting microstructure can be significantly altered. A multi-scale numerical model captures the meso-scale melt pool dynamics coupled to microscale solidification showing the microstructure evolution and solute redistribution. The results highlight the complex interaction of the various physical phenomena and also show the method's potential to disrupt the epitaxial growth defect. The model predictions are supported by preliminary experimental results that demonstrate the dependency of the melt pool depth on magnetic field orientation. The results highlight how a time-dependent field has the potential to provide an independent control mechanism to tailor microstructures.

1. Introduction

Additive Manufacturing (AM), also known as 3D printing of alloys is an emerging technology with tremendous potential in a wide range of sectors including energy, biomedical implants and aerospace [1-3]. However, unlike traditional casting methods with centuries of development, AM has yet to reach the same level of maturity and suffers from microstructural defects such as porosity and epitaxial growth [4-7]. The latter, leading to the formation of long grains and unwanted anisotropic properties. These microstructural features are related to the melt pool dynamics and heat transfer, which in turn are governed by complex physics such as radiation[8], evaporation[9] and intense convection from temperature dependent Marangoni flow[10]. The thermal Péclet number is generally much greater than unity in AM processes, so that the heat transfer and corresponding melt pool morphology are strongly dependent on the fluid dynamics in the melt pool. Controlling the melt pool dynamics is therefore critical to beneficially tailor the resulting microstructure and mitigate against defects. One method that is receiving increased attention is the application of an external magnetic field [11]. Magnetic fields are often used to introduce the electromagnetic damping force on liquid flow, however, in many AM and related welding processes, large thermal gradients are present and conducive to the formation of Thermoelectric (TE) currents [12]. These currents interact with the magnetic field generating a TE Lorentz force that drives fluid flow in the melt pool alongside other inherent fluid drivers such as buoyancy and Marangoni stress. The TE Lorentz force is dependent on the time-dependent orientation and magnitude of the magnetic field and therefore, the introduction of a magnetic field strategy in

conjunction with the scanning strategy brings a truly independent mechanism to control AM processes and the resulting microstructure.

Previous work by the authors [13,14] showed this strong dependency of the orientation of the magnetic field on the melt pool depth and solute redistribution. In these previous works quasi-steady state solutions for the thermofluid problem were first solved and used as an input to predict microstructure evolution. Nie et al. [15] concluded that static magnetic field causes EM braking which then suppresses meltpool convection and allows the melt to redistribute between dendrites during remelting therefore reducing residual stresses. Yeung and Yan [16] demonstrated a successful meltpool size control by laser power tuning that is based on a data-driven predictive meltpool model. Mondal et al. [17] developed a hybrid framework that uses machine learning to model and optimize the meltpool geometry control. Wang and Yan [18] considered a free surface and induced magnetic field in their TEMHD model simulations and concluded that the induced magnetic field impact is negligible compared to an externally applied magnetic field. Gruzd et al. [19] presented a theoretical assessment of the effect of an alternating EM field on meltpool convection for the purpose of stainless-steel laser annealing. They concluded that the TE effect is much smaller for stainless steel than it is for aluminium alloys. Du et al. [20] studied the effects of an external magnetic field in laser powder bed fusion and reaffirmed the positive impact on material physical properties and the importance of TE Lorentz force on the meltpool flow dynamics.

In this paper we further expand on this work by coupling time dependent solutions between the mesoscopic thermofluid problem and microstructure evolution, to investigate the influence of a time-dependent magnetic field on the modulation of the melt pool.

2. Methodology

A numerical model representing the Selective Laser Melting (SLM) AM process has been developed. The model uses a multi-scale approach where on the mesoscale an Enthalpy based approach captures solidification and heat transfer, from this a staggered finite difference method resolves the thermoelectric currents, which are then used to calculate the thermoelectric force that appears as a source term in the Lattice Boltzmann method to capture TEMHD flow. Time dependent solutions of the temperature and velocity are then coupled to a microscale model that uses a Cellular Automata method based on the code μMatIC [21-23], to resolve solute redistribution and microstructure evolution. The mesoscale solutions have a resolution of 5 μm, while the microscale is resolved at 1 μm. A more detailed description of the method can be found in Kao *et al.* [13], however a summary of the governing equations begins with modified form of Ohm's law accounting for TE currents

$$\mathbf{J} = \sigma(\mathbf{E} - S\nabla T + \mathbf{u} \times \mathbf{B}), \tag{1}$$

where $\mathbf{J}$ is the current density, σ is the electrical conductivity, S is the Seebeck coefficient, T is the temperature, $\mathbf{u}$ the fluid velocity and $\mathbf{B}$ the magnetic field. The Lorentz force, $\mathbf{F} = \mathbf{J} \times \mathbf{B}$ then appears as a source term in the Navier-Stokes equation governing fluid flow

$$\rho\left(\frac{\partial \mathbf{u}}{\partial t} + \mathbf{u} \cdot \nabla \mathbf{u}\right) = -\nabla p + \mu \nabla^2 \mathbf{u} + \mathbf{J} \times \mathbf{B}, \tag{2}$$

where ρ is the density, t is time, p is pressure and μ is the dynamic viscosity. The solutions to (1) and (2) also satisfy continuity of mass and charge, $\nabla \cdot \mathbf{u} = \nabla \cdot \mathbf{J} = 0$. In this work the magnetic field is oriented in the $\hat{y}$-direction, transverse to the scan, $\hat{x}$-direction, and build, $\hat{z}$-direction, and varies sinusoidally in time as $B_y = B_0 \sin(2\pi t f)\, \hat{y}$, where B_0 is the amplitude of the magnetic field and f is the frequency of its oscillation. Velocity is used to calculate time-dependent convection for both temperature, T, and concentration, C. The heat transfer is given by

$$\frac{\partial T}{\partial t} + \mathbf{u} \cdot \nabla T = \nabla \cdot \alpha \nabla T, \tag{3}$$

where α is the thermal diffusivity. In the mesoscale Enthalpy model the latent heat of fusion L_f is related to the temperature using the volumetric enthalpy H by

$$H = (1 - \phi_s)L_f + c_p T, \tag{4}$$

where ϕ_s is the solid fraction and $c_p$the specific heat capacity. For the CA method the solid fraction concentration of solute in the solid, C_s, and liquid, C_l are governed by $C_s = kC_l$, where k is the partition coefficient of the solute. The concept of solute trapping is used to account for both the physical non-equilibrium effect, but also a numerical effect where the computational resolution is much coarser than the interdendritic spacing. Each cell is considered to be the average of both high concentration eutectic structures and dendrites. The Continuous Growth Model [24] corrects for this by proposing a modification of k given by

$$k = \frac{k_e + V/V_D}{1 + V/V_D}, \tag{5}$$

where V is the growth velocity and $V_D$the 'diffusion' velocity. In this case $V = u_s$is the scan velocity and $V_D \approx D_l/L$ where L is a characteristic length, typically the interface thickness, but to account for numerical trapping assumed much larger, close to the cell size, giving a value of k = 0.95 [13]. At the solid-liquid interface the solid fraction rate of change is calculated by

$$C_l(1-k)\frac{\partial \phi_s}{\partial t} = -\nabla \cdot (D_e \nabla C_l) + [1 - (1-k)\phi_s]\frac{\partial C_l}{dt}, \tag{6}$$

where $D_e = (1 - \phi_s)D_l + \phi_s D_s$is the equivalent diffusion coefficient and $T_i = m_l(C_l - C_0)$ is the interface equilibrium temperature with m_l the liquidus slope and $C_0$the reference concentration. The equivalent $C_e = (1 - \phi_s)C_l + \phi_s C_s$

$$\frac{\partial C_e}{\partial t} + \mathbf{u} \cdot \nabla C_l = \nabla \cdot D_e \nabla C_l, \tag{7}$$

with zero mass flux prescribed at the boundaries.

The Navier-Stokes equation (2) are solved using the Lattice Boltzmann Method (LBM) [14, 25,26]. The other equations (1), (3-4) and (6-7), are solved using finite difference method schemes [27, 28]. The equations are solved throughout the whole domain.

The multiple pass layers of the AM process are captured by using offset periodic boundary conditions at each edge. A moving mesh approach is used with solidified material leaving the domain at the back and entering the layer below. A new powder layer is then introduced at the front of the first layer. A schematic of this can be seen in figure 1. The computational domain is cuboid with dimensions 800 × 600 × 300 µm and the incoming powder layer has a height of 30 µm. With a scan speed of 0.1 m/s and a domain length of 800 µm incoming material will be re-introduced into the layer below after 8 ms and

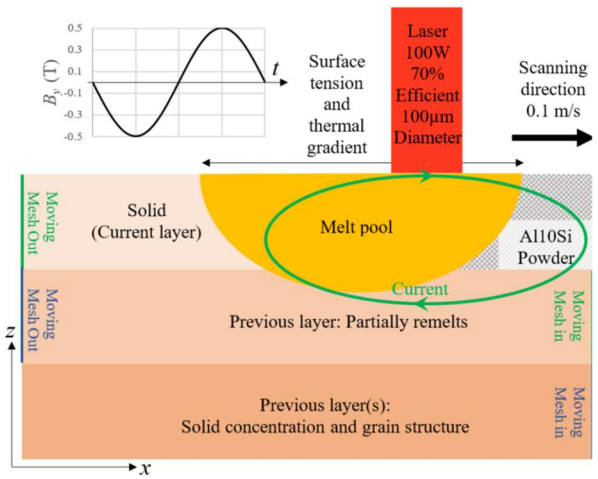

Figure 1. Schematic of the AM process, highlighting the TE current circulation. the moving mesh and the oscillating B_y field.

corresponds to a characteristic magnetic field frequency of ~100 Hz, assuming an oscillation occurs within a single layer. While this may be impractical experimentally and the induced currents from the time dependent field are neglected in the model, it is necessary to see the influence on successive layers without modelling a domain that is 100 to 1000 times larger. Newton's second law with a predicted Lorentz force as high as 10^8 N/m^3, gives ~10 μs as an estimate of the characteristic time for acceleration, several orders of magnitude smaller than the time scale for material to be re-introduced into the domain.

3. Results

In our previous work [13,14], numerical models predicted that application of a magnetic field aligned transverse to the build and scan directions, would interact with the dominant current density, in the scan direction, to generate a Lorentz force in the build direction i.e. $\mathbf{J} \times \mathbf{B} \sim J_x B_y \hat{z}$. This force was greatest near the laser spot and depending on the sign of the magnetic field it would either be directed upwards towards the surface of the melt pool reinforcing Marangoni flow or downwards competing against it. The resultant melt pool morphology then became either shallower (and wider) or deeper (and narrower).

Recent experiments conducted on the related Directed Energy Deposition (DED) process have shown strong evidence of the predicted mechanisms. Figure 2 shows bi-directional scanning for 5 layers of AlSi10 in the DED processes with a laser power of 200 W and a scan speed of 1 mm/s. Further details of the underlying experimental set up are reported by Chen *et. al* [29]. In this case the magnetic field is fixed, however the bi-directional scanning (left to right followed by right to left etc.) shares similarities to changing the sign of the magnetic field per layer. By alternating the scan direction, the thermoelectric

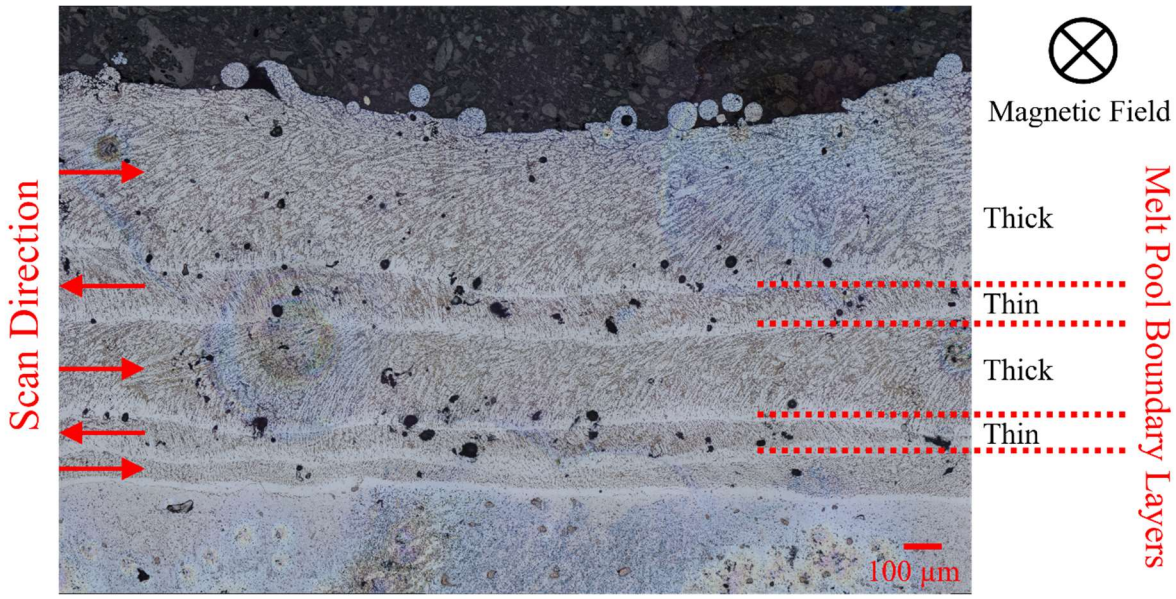

Figure 2. Experimental results demonstrating the effect of bidirectional scanning in the presence of a transverse magnetic field.

currents change sign, hence the Lorentz force changes sign. The melt pool boundary layers are clearly visible and indicated in the figure by regions of relatively parallel lighter lines and provide an indication of the depth of the melt pool. Except for the first layer that is printing onto the substrate, the experiment shows how the distance between successive melt pool boundary layers alternates between thick – thin – thick etc., giving the same predicted behaviour as if the melt pool was alternating between deep – shallow etc. for each layer.

The numerical modelling presented in this work uses an oscillating magnetic field which causes an oscillating force and modulation of TEMHD in the melt pool. Figure 3 shows the temperature field and melt pool morphology at different phases of the magnetic field. Figure 3a shows when the magnetic

field is at a minimum, $B_y = -0.5$ T and the force is negative giving a deep meltpool, figure 3b is when $B_y = 0$ T and figure 3c is when $B_y = +0.5$ T and at a maximum with a shallow meltpool.

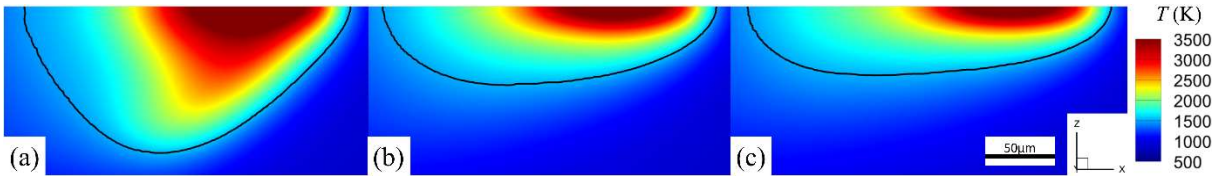

Figure 3. Melt pool temperature cross sections for various phases of the magnetic field with B_y intensities of a) 0.5 T, b) 0 T and c) - 0.5 T.

Figures 4, 5 and 6 show results for an oscillating magnetic field with a frequency matching the period of two layers, 62.5 Hz. Each figure shows the concentration and grain structure in different planes. Figure 4 shows the scan-build plane (x-z), figure 5 the scan-transverse plane (x-y) and figure 6 the transverse-build plane (y-z). The location of the slices taken for figures 5 and 6 are indicated in figure 4. In this case the region where the magnetic field is positive and negative overlap with the shallow positive magnetic field being remelted by the deeper negative magnetic field regions. Similar to the results in our previous work [13], in Figure 4 the low concentration melt pool boundary layer is evident showing the history over successive layers. The layers are uneven in thickness, since when the melt pool is deep it remelts through previous layers, while at the edges of the figure the magnetic field is tending toward zero leaving a shallower and hence thinner region between the melt pool boundary layers. The solute concentration in the vicinity of the melt pool boundary layer increases as the magnetic field tends to zero, while this effect is not seen in this region where the magnetic field is applied. This variation in concentration is due to TEMHD flow competing with Marangoni flow, at the edges, where the magnetic field is low, Marangoni flow dominates sweeping the flow towards the centre of the melt pool and hence the high concentration regions. In the centre of figure 4, TEMHD flow dominates and flow is pushed to the bottom of the melt pool and swept to the sides. This effect can be seen in the melt pool in figure 6a, but also in figure 5a, where high concentration regions in the solidified structure can been seen off the centre line, an indication that the solute was captured at the sides of the melt pool. Figure 5a also shows three meltpool boundary layers, starting from the centre of the figure and moving outwards these are: an intersection with the bottom of the deep melt pool of the topmost layer, the second is the boundary from previous time the melt pool was deep and thinner (two layers before), while the furthest is from the previous layer when the magnetic field causes a shallow wide melt pool.

Figure 4b shows long epitaxial grains can be seen in the regions where the magnetic field is applied, central to the figure, while at the edges there is a ‘wavey’ like structure. Grains compete and typically those whose orientation aligns with the thermal field will win this competition. However, as the thermal field is also oscillating the preferred orientation changes with time giving rise to complex competition that may be able to prevent epitaxial growth in certain regions. This disruption to epitaxial growth is also evident in the scan-transverse section given in figure 5a and 5b, where due to remelting through successive layers the thermal field and hence gradient during re-solidification is very different and favours different grain orientation. There is a clear disruption to epitaxial growth, in the region of the superimposed ‘oval’ in figure 5b, that matches the meltpool boundary layer of figure 5a. In the region where the magnetic field is applied, Figure 4a, shows long grains formed from epitaxial growth. However, figure 6b shows that these grains are quite ‘thin’ and are a consequence of scanning in the same location between each layer.

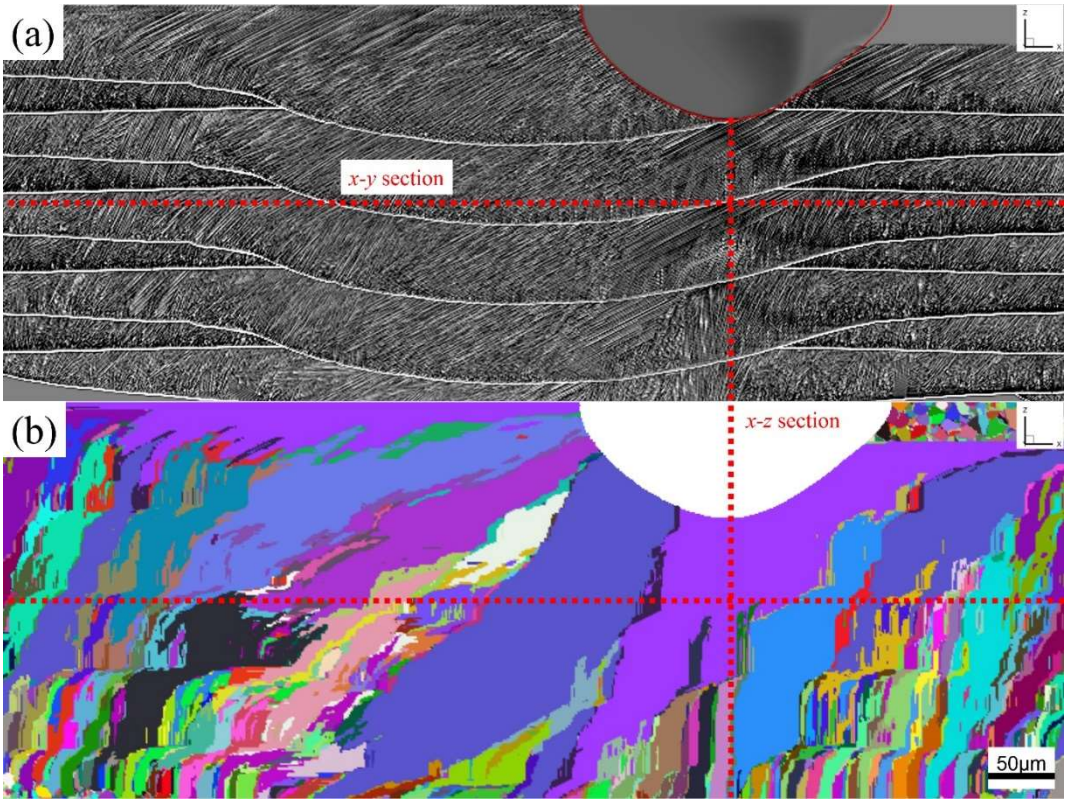

Figure 4. Concentration – dark/light regions are solute enriched/depleted respectively (a) and Grain Structure (b) for the scan-build plane (x-z) for a B_y field frequency 62.5 Hz.

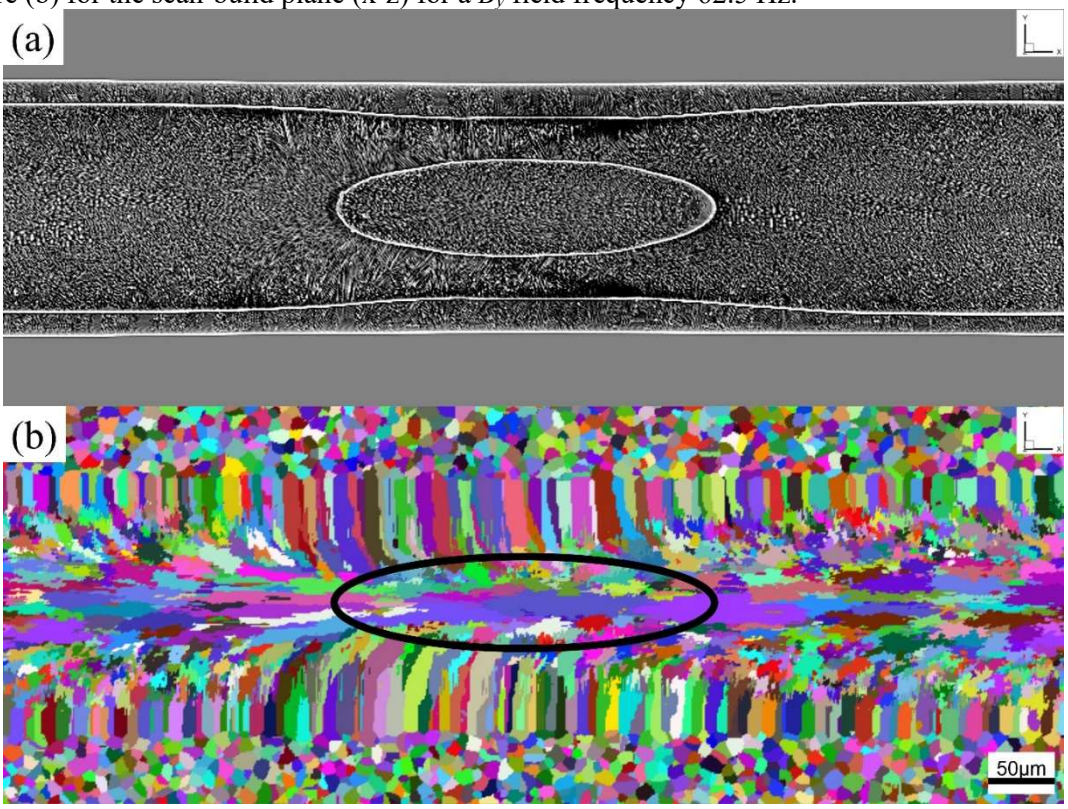

Figure 5. Concentration – dark/light regions are solute enriched/depleted respectively (a) and Grain Structure (b) for the scan-transverse plane (x-y) for a B_y field frequency 62.5 Hz.

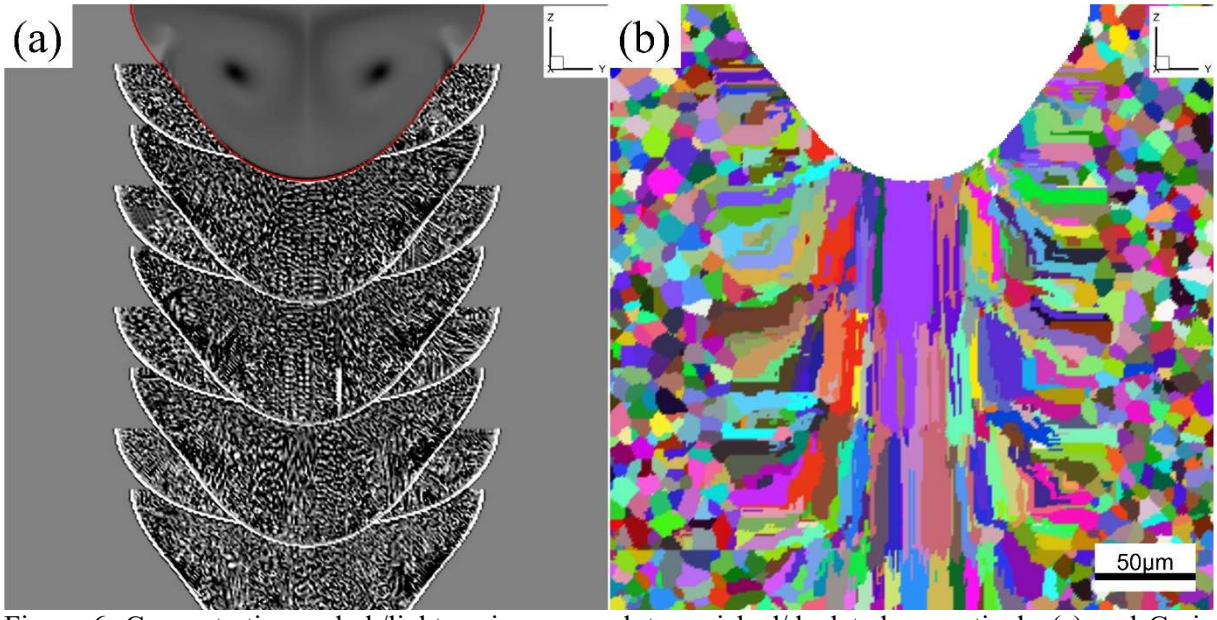

Figure 6. Concentration – dark/light regions are solute enriched/depleted respectively (a) and Grain Structure (b) for the transverse-build plane (y-z) for a B_y field frequency 62.5 Hz.

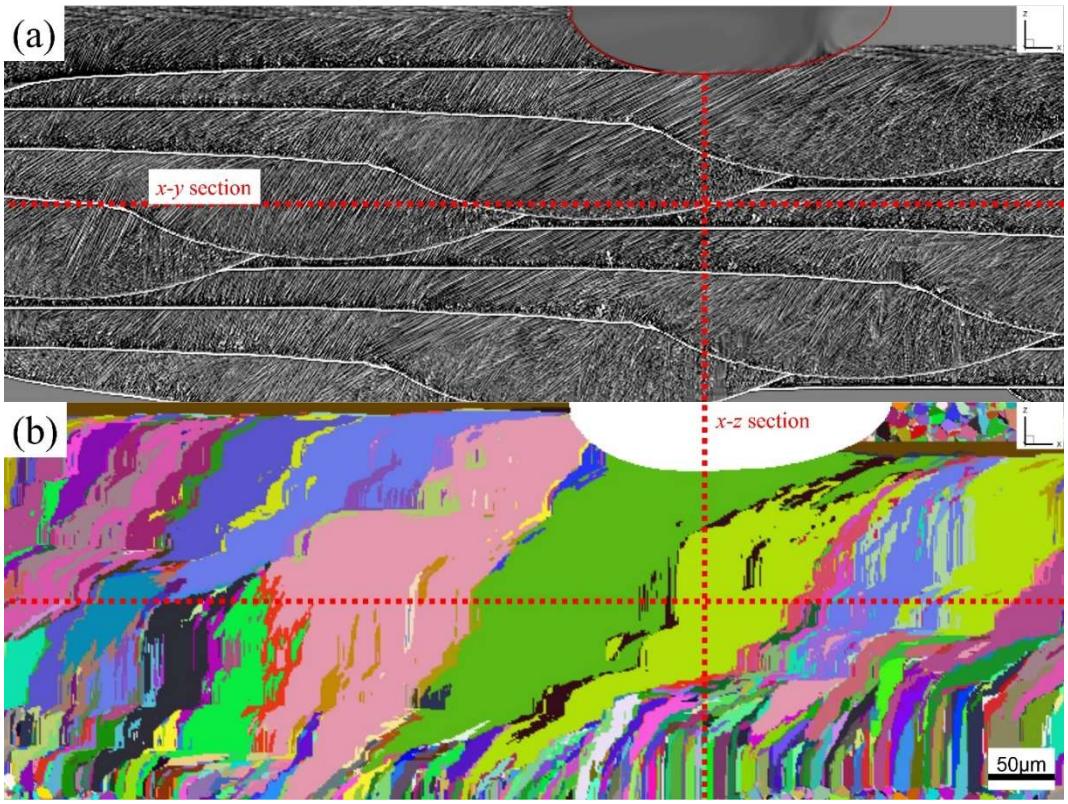

Figure 7. Concentration – dark/light regions are solute enriched/depleted respectively (a) and Grain Structure (b) for the scan-build plane (x-z) for a B_y field frequency 100 Hz

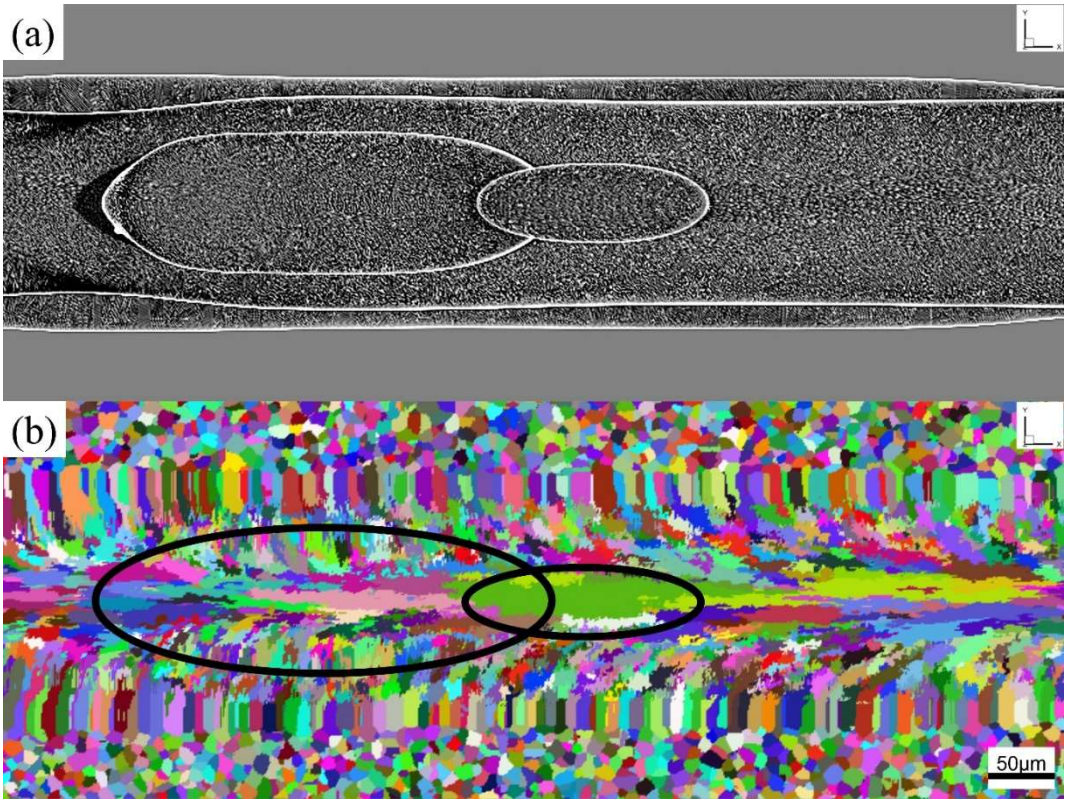

Figure 8. Concentration – dark/light regions are solute enriched/depleted respectively (a) and Grain Structure (b) for the scan-transverse plane (x-y) for a B_y field frequency 100 Hz

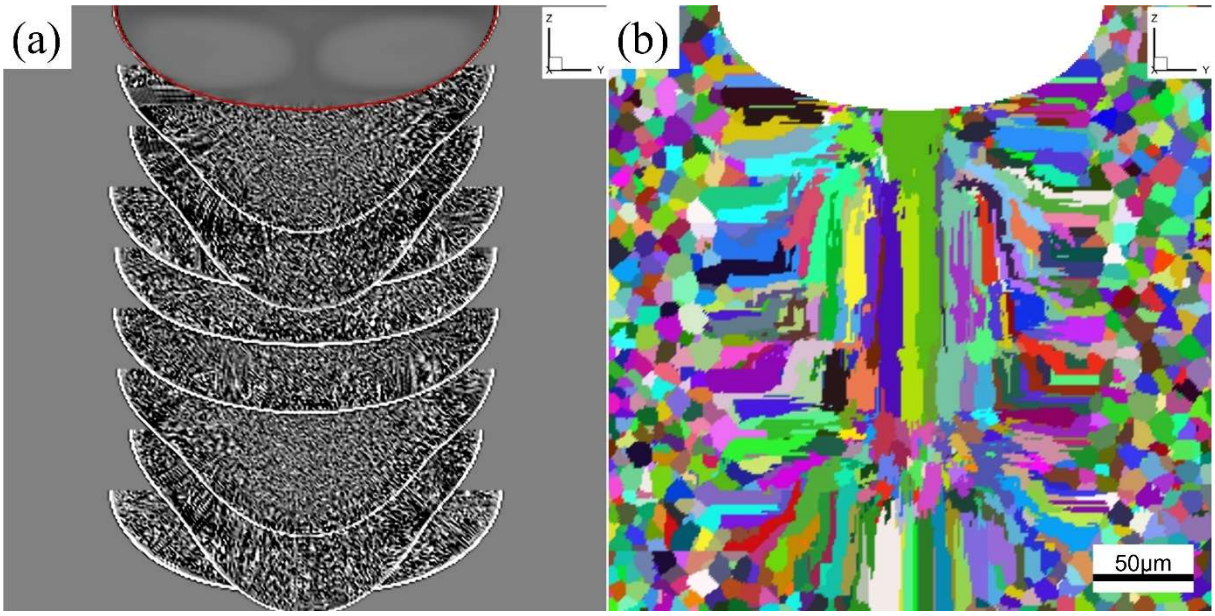

Figure 9. Concentration – dark/light regions are solute enriched/depleted respectively (a) and Grain Structure (b) for the transverse-build plane (y-z) for a B_y field frequency 100 Hz

The second case shown is with a high frequency of 100 Hz such that the positive and negative magnetic fields are not in the same relative location. Figures 7,8 and 9 are relevant to this case where again each figure shows the concentration and grain structure in different planes. Figures 7, 8 and 9 shows the scan-build plane (x-z), the scan-transverse plane (x-y) and the transverse-build plane (y-z), respectively and the locations are again indicated in figure 7. Due to the shift in position where the deep meltpool acts, figure 7a shows how the meltpool boundary layers take a much more complex structure, where intersections due to remelting of previous layers leads to a much more disparate distance between melt pool boundary layers. Regions of high concentration are more distributed throughout the domain due to the varying position where Marangoni flow dominates and solute is drawn to the centre of the melt pool, highlighted in the solute redistribution in the melt pool of figure 9a. On the grain structure, figure 7b, shows how the epitaxial growth appears to follow the shift in position of regions of high magnetic field, however looking in the other planes there are additional mechanisms for disruption of epitaxial growth. An example is in the scan-transverse section shown in figure 8, where the slice cuts through the bottom of two successive deep melt pools, indicated by the melt pool boundary layers in figure 8a and the two superimposed ovals in figure 8b. In a similar way to the previous case, the thermal field is contrasting during remelting and re-solidification, leading to a complex grain competition and the disruption of epitaxial growth. Another example is in the transverse-build plane, shown in figure 10b, where in the lower portion of the figure there is a region of small grains dissecting the longer grains. This is again due to the difference in thermal gradient during solidification. When the thermal gradient is more vertical, the preferred orientation would also be vertical and likewise when the thermal gradient is horizontal the preferred orientation would be horizontal. This change in grain morphology is essentially where epitaxial growth is disrupted, oriented more vertically to those further up that are more horizontal. This case highlights how a more complex and interesting behaviour of the microstructure evolution can be achieved by modulating the magnetic field and hence the thermofluid problem.

4. Conclusions

Experimental results in the related DED system have been shown to verify early predictions of how melt pool depth can be changed with a magnetic field. Further numerical predictions in this work have then gone to investigate the effect of a low frequency oscillating transverse magnetic field on the melt pool dynamics and grain morphology of SLM AM aluminium. The time-dependent magnetic field interacts with the TE currents in the melt pool leading to a modulation of TEMHD and ultimately modulation of the meltpool morphology through convective transport. Due to the synchronised spatial and temporal nature of the cases presented, the time-dependent melt pool morphology leads to spatial variations in the layer thickness and solute redistribution, as TEMHD competes with or enhances Marangoni flow. A host of other microstructure effects such as complex grain competition due to the varying thermal gradient at solidification leads to regions of enhanced or disrupted epitaxial growth. By simply changing the frequency of the magnetic field, so that the intensity is not in the same relative place at each layer, created an even more complex final microstructure, that warrants further analysis. This study also demonstrates that the parameter space for the magnetic field strategy is large and therefore could have a huge potential in tailoring microstructures by optimising a combined magnetic field and scan strategy.

Acknowledgements

The authors acknowledge financial support from the UK Engineering and Physical Sciences Research Council (EPSRC) through grants EP/W032147/1 and EP/W031167/1.

References

[1] Singh R, Lee P D, Dashwood R J and Lindley T C 2010. *Mater. Technol.* **25** 127–36
[2] Ibrahim K A, Wu B and Brandon N P 2016 *Mat. Des.* **106** 51–9
[3] Murr L E 2016 J. *Mat. Sci. Tech.* **32** 987–95
[4] Zhang B, Li Y and Bai Q 2017 *Chinese J. Mech. Eng.* **30** 515–27
[5] Leung C L A, Marussi S, Atwood R C, Towrie M, Withers P J, Lee P D 2018 *Nat. Comm.* **9** 1355

[6] Li R, Shi Y, Wang Z, Wang L, Liu J and Jiang W 2010 *Appl. Surf. Sci.* **256** 4350–6
[7] Shifeng W, Shuai L, Qingsong W, Yan C, Sheng Z and Yusheng S 2014 *J. Mater. Process. Technol.* **214** 2660–7
[8] Gusarov A, Yadroitsev I, Bertrand P and Smurov I 2009 *J. Heat Transfer* **131** 072101
[9] Geiger M, Leitz K H, Koch H and Otto A 2009 *Prod. Eng.* **3** 127–36
[10] Yuan P and Gu D 2015 *J. Phys. D: Appl. Phys*. **48** 035303
[11] Du D, Haley J C, Dong A, Fautrelle Y, Shu D, Zhu G, Li X, Sun B and Lavernia E J 2019 *Mat. Des.* **181** 107923
[12] Kern M, Berger P, Hugel H. 2000 Magneto-fluid dynamic control of seam quality in CO2 laserbeam welding. Weld. J. Res. Suppl. 79, 72s.
[13] Kao A, Gan T, Tonry C, Krastins I and Pericleous K 2020 *Philos. Trans. Royal Soc. A* **378** 2171
[14] Kao A, Gan T, Tonry C, Krastins I and Pericleous K 2020 IOP Conf. Series: Mat. Sci. and Eng. **861** 012009
[15] Nie J, Chen C, Shuai S, Lui X, Zhao R, Wang J, Liao H and Ren Z 2020 *J. Therm. Spray Technol.* **29** 1410–1423
[16] Yeung H, Yang Z and Yan L 2020 *Addit. Manuf.* **35** 101383
[17] Mondal S, Gwynn D, Ray A and Basak A 2020 *Metals* **10(5)** 683
[18] Wang L and Yan W 2021 *Phys. Rev. Applied* **15** 064051
[19] Gruzd S, Lomaev S, Simakov N, Gordeev G, Bychkov A, Gapeev A, Cherepetskaya E, Krivilyov M, Ivanov I 2022 *Metals* **12(9)** 1540
[20] Du D, Wang L, Dong A, Yan W, Zhu G, Sun B 2022 *Int. J. Mach. Tools Manuf.* **183** 103965
[21] Wang W, Lee P and McLean M 2003 *Acta Mater*. **51** 2971–87
[22] Yuan L and Lee P D 2010 *Modell. Simul. Mater. Sci. Eng.* **18** 055008
[23] Yuan L and Lee P D 2012 *Acta Mater.* **60** 4917–26
[24] Aziz M J and Kaplan T 1988 *Acta Metall.* **36** 2335–47
[25] Kao A, Krastins I, Alexandrakis M, Shevchenko N, Eckert S, Pericleous K 2018 *JOM* **71** 48–58.
[26] Kao A, Shevchenko N, Alexandrakis M, Krastins I, Eckert S and Pericleous K 2019 *Philos. Trans. Royal Soc. A* **377** 20180206
[27] Kao A, Cai B, Lee P and Pericleous K 2017 *J. Cryst. Growth* **457** 270–4
[28] Voller V R, Cross M and Markatos N C 1987 *Int. J. Numer. Methods Eng.* **24** 271–84
[29] Chen Y, Clark S J, Sinclair L, Leung CLA, Marussi S, Connolley T, Atwood RC, Baxter GJ, Jones MA, Todd I and Lee PD 2021 Addit. Manuf. 41 101969.